Lawrence Berkeley National Laboratory
Materials Sciences

Title
The Effects of Native Oxide Surface Layer on the Electrochemical Performance of Si Nanoparticle-Based Electrodes

Authors
Xun, S
Song, X
Wang, L
et al.

The Effects of Native Oxide Surface Layer on the Electrochemical Performance of

Si Nanoparticle-Based Electrodes

S. Xun[1], X. Song[1], Lei Wang[1], M. E. Grass[2], Z. Liu[2], V. S. Battaglia[1] & G. Liu[1, z]

[1] Environmental Energy Technologies Division

[2] Advanced Light Source

Lawrence Berkeley National Laboratory

Berkeley, CA 94720

USA

[z] Corresponding Author

Phone (510) 486-7207

Fax (510) 486-7303

Email: gliu@lbl.gov

Abstract

This study controllably reduces the silicon dioxide (SiO_2) layer on Si nanoparticles and evaluates its effect on the performance of Si nanoparticle-based electrodes in Li-ion batteries. Various thicknesses of this native oxide are present on Si nanoparticles generated by chemical vapor deposition (CVD) due to the process conditions and exposure to oxygen during storage. This layer can be effectively reduced by hydrofluoric acid (HF) etching, which results in improved electrochemical performance over as-received samples. As-received Si sample has a higher first-cycle capacity loss than that of the etched Si samples, when the capacity loss is normalized to the surface area of the Si particles. Spectroscopic analysis reveals that when the Si electrode is held at a low potential, the oxide layer can be converted to a more stable silicate form due to the irreversible consumption of lithium species in the cell. The thick SiO_2 surface layer also isolates the Si core from lithium-ion alloying; therefore, the as-received Si nanoparticles deliver a lower specific capacity than their etched counterpart. Incomplete lithiation of the as-received Si particles is confirmed by transmission electron microscopy, which shows that nanocrystalline Si domains remain after cycling. The surface insulating effects of SiO_2 also cause high impedance in the Si electrode.

Introduction

Si nanoparticles of various forms, such as spheres, wires or tubes, are being developed as lithium-ion storage materials or capacity boosters in combination with graphite in the lithium-ion negative electrode. Although the theoretical specific capacity of Si (3579 mAh/g at $Li_{15}Si_4$)[1, 2] is almost 10 times higher than that of graphite (372 mAh/g), poor capacity retention due to the volume change during the lithiation and delithiation process hinders its practical application. Nanosizing Si particles has proven to be an effective strategy for extending the cycle life of Si-based electrodes.[3-10] However, the increased surface area due to nanosizing of the particles causes a dramatic increase in surface-based side reactions. The electrolyte can be reduced on the surface of Si nanoparticles to form a solid-electrolyte interface (SEI) layer during initial cycling and can continue reacting in the following cycles, leading to the loss of lithium-ion species.

Another possible reason for the initial capacity loss is the reduction of the SiO_2 layer, which is typically found on most of the Si surface. However, there is still debate on the actual reaction pathway and final product resulting from the conversion of the SiO_2 layer. Huang et al. reported that the strong Si-O bond cannot be broken by reaction with lithium-ion under normal operating conditions of the negative electrode (0.01-1 V Li/Li$^+$), thus SiO_2 remains intact during electrochemical cycling.[11] Larcher et al. claimed that the potential must be about 1 V below the equilibrium potential to trigger Reaction (1), and, accordingly, the reduction of SiO_2 to Si and Li_2O is kinetically impossible.[12]

$$SiO_2 + 4Li \quad \rightarrow \quad Si + 2Li_2O \qquad E_0 = 0.69\ V \quad (1)$$
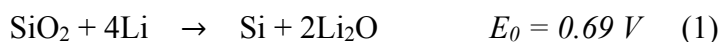
On the contrary, Fultz et al. claimed that reduction of SiO_2 by lithium is thermodynamically favorable, likely resulting in a higher first cycle irreversible

3

capacity.[5] Wang et al. reported electrochemical reduction of nano-SiO_2 in hard carbon with Li_4SiO_4 and Li_2O as the products, as proven by solid-state nuclear magnetic resonance (NMR) and X-ray photoelectron spectroscopy (XPS).[13] In addition, Fu et al. fabricated and tested SiO_2 thin-film electrodes to demonstrate the lithium-ion storage properties, and used XPS and TEM measurements to propose $Li_2Si_2O_5$ as the reduction product instead of an inert Li_2O.[14] These early reports provide a glimmer of the possible transformation of SiO_2 on the Si nanoparticle surface during electrochemical processes. In most of these reports, however, the electrode is operated between 0-3 V (Li/Li$^+$), and rate control is not being considered as a factor during the cell operation. More controlled experiments that resemble the operating conditions of lithium-ion negative electrodes have not been reported.

We previously reported that the SiO_2 layer on Si nanoparticles can be controllably reduced to different thicknesses.[15] Results indicated that the reversible capacity of Si-based electrodes could be enhanced by reducing the SiO_2 thickness. This paper reports a systematic study of the effect of SiO_2 surface layers on the electrochemical performance of Si nanoparticles, and the conditions for reduction of this SiO_2 layer in a lithium-ion negative electrode.

Experimental

Materials used in this study, the procedure for reduction of oxide layer, and XPS measurement methods were reported previously.[15] The SiO_2 content of the commercial Si nanoparticles was measured with elemental analysis method provided by Columbia

Analytical Services in the Tucson Laboratory. The composition of Si/acetylene black (AB)/polyvinylidene difluoride (PVDF) (1:2:1 weight ratio) was used in this study. The laminates and coin cell assembly were prepared according to a previously reported method.[15-17] Lithium metal was used as the counter electrode. The coin cell performance was evaluated with a Maccor Series 4000 Battery Test System in a thermal chamber at 30°C. The coin cells were cycled at C/10 current density between 1V and 0.01 V unless otherwise specified. Infrared spectra were recorded with a Nicolet 710 FTIR spectrometer in transmission mode. To make data comparative, the concentration of different Si particles in KBr was fixed at 0.17 wt% and 0.1 g of mixture was pressed to a pellet with a diameter of 1.3 cm. A 200 kV FEI monochromated F20 UT Tecnai was used to produce high-resolution TEM images of the Si nanoparticles. The morphology of electrodes was imaged with a JEOL JSM-7500F field emission scanning electron microscope (SEM). The powder specific surface areas were measured by a Brunauer-Emment-Teller (BET) N_2 adsorption method with a Micromeritics tristar surface area and porosity analyzer. Electrochemical impedance spectroscopy (EIS) measurements were performed using a VMP3 BioLogic electrochemical workstation with a frequency range from 30 KHz to 0.01 Hz.

Results and Discussion

Morphology and surface area before and after HF etching. – The silicon nanoparticles synthesized by CVD have a fused particle structure and an average particle size of 50 nm with a large size distribution (Fig. 1). The core-shell structure is clearly visible in the as-received sample. The shell is an amorphous SiO_2 with a nanocrystalline Si core. The SiO_2

content of this sample is very high (27% by weight), and the coverage is not uniform throughout the particle.[15] This Si material is intentionally chosen to amplify the effect of this surface oxide layer on its electrochemical performance, and later for the ease of controlled removal of the layer. The individual particles appear to fuse together by the outer SiO_2 layer.

HF etching not only removes the oxide layer from the particle surface, but also dramatically changes the morphology of the particles. The particles are no longer fused and are separated into individual particles after HF etching. The surface oxide reduction also dramatically changes the surface area of the Si samples. The surface areas of different particles were measured by BET, as shown in Table I. BET surface areas for as-received, 10 min-etched, and 30 min-etched Si are 37.92, 76.82, and 136.19 $m^2\ g^{-1}$, respectively. Assuming the particles are spherical and based on Equation (2), where ρ is the density and a is the BET measured surface area, the calculated particle diameters, d, for as-received, 10 min-etched, and 30 min-etched Si are 68, 33, and 19 nm, respectively.

$$d = 6/(\rho \times a) \qquad (2)$$

As measured by XPS, a 6.2 nm-thick oxide layer is found on as-received Si. Thus, even if all the SiO_2 was removed, the diameter of the particle should be 55.52 nm (67.92-2×6.2), which is much bigger than the 19 nm derived based on BET measurement. Also, observed particle sizes are mostly unchanged based on the TEM images of the etched sample. The reason for the discrepancy between expected and derived diameters is that the dissociation of the fused particles generates more surface area. There are also much

6

smaller Si nanoparticle aggregates formed after HF etching, which may significantly contribute to the increase of specific surface area (Fig. 1). XPS measurements revealed that the thickness of the native oxide layer decreases to 2.7 and 1.3 nm after 10 min and 30 min of HF etching, respectively. This oxide reduction method is a reliable process for generating Si nanoparticles with different oxide layer thicknesses for our study on the surface effect of Si materials.

Surface composition before and after HF etching. – Besides the significant oxide reduction visualized by TEM and detected by XPS experiments, information on the surface chemistry of the Si particles before and after HF etching can be obtained by FTIR measurement. The spectra in Fig. 2 are normalized based on the loading of Si samples . The peaks in the range of 900-1250 cm^{-1} correspond to Si-O-Si stretching.[18] The main peak intensity decreases as HF etching time increases, indicating that the SiO_2 was removed significantly. In addition, a slight shift of the stretching band to lower frequencies is observed as etching time increases, which may be caused by a decrease in the surface oxide layer. For both the as-received and etched samples, the absence of a silanol (Si-OH) peak at 3670 cm^{-1} confirms the absence of a hydroxide terminate surface.[19] Both as-received and etched samples went through a vacuum drying process at 120°C for 12 hours. This drying process causes condensation and dehydration of surface hydroxide, leading to the oxide-terminated surface. The broad absorption peak at 3400 cm^{-1} shown in Fig. 2 indicates the existence of hydrogen bonded -OH groups. This peak intensity decreases with the reduction of the SiO_2 layer, indicating that the -OH groups

7

are associated with the SiO_2 layer. The surface -OH content is one of the factors contributing to capacity loss during the first charge cycle.[20, 21]

First cycle loss of the Si electrode for different thicknesses of SiO_2. – Fig. 3 plots the initial cycling performance of the Si nanoparticles with different oxide coverage. The capacity is normalized to Si content after deduction of surface SiO_2 content. Since the electrode was loaded with AB to increase electronic contact to Si nanoparticles, the AB cycling behavior was studied and found to have both irreversible and reversible capacity. The irreversible capacity of Si nanoparticles after deduction of AB irreversible capacity is listed in Table II. Since the irreversible capacity is related to the surface area, the surface areas of the Si active materials were measured by BET. The irreversible capacity of Si materials based on particle surface area are calculated and shown in Table II. The area-specific irreversible capacities based on the Si surface decrease when the surface oxide is systematically removed, indicating that the surface oxide plays a key role in the first cycle loss.

The irreversible capacity is mainly caused by the reduction of electrolyte on the electrode surface to form an SEI layer. In this case, all the particles possess a native SiO_2 layer with different thickness. Thus, the first concern is whether the surface SiO_2 with different thickness causes different SEI formation. Fig. 4 shows the dQ/dV curves of the first discharge profile (0.2 -2.2 V) based on the cells with as-received and 30 min-etched Si with a constant discharge rate of 0.1C (ca. 125 μA cm^{-2}). Three peaks associated with electrolyte decomposition on Si and AB are observed for both electrodes. No difference

8

can be distinguished from the spectra, indicating that similar surface reactions occur in this potential range during the first cycle for both as-received and etched Si materials.

To understand SEI formation chemistry, the electrodes based on as-received and 30 min-etched Si were examined after 1 cycle of lithiation and delithiation between 1-0.01 V. The cycled electrodes were rinsed with pure dimethylcarbonate and dried thoroughly before SEM and energy-dispersive X-ray spectroscopy (EDX) were conducted to investigate the morphology and elemental ratio changes of the electrodes. The fresh electrodes based on as-received Si and 30 min-etched Si were also studied for comparison. SEM images of the electrodes before and after cycle are shown in Fig. 5. The aggregation of Si particles in a fresh electrode based on as-received Si is observed (Fig. 5a). In contrast, no Si particle aggregation in the electrode based on 30 min-etched Si (Fig. 5b) is observed. These observations are consistent with TEM observations of particles before and after etching (Fig. 1). No visible differences are found between the surfaces of cycled electrodes based on as-received Si (Fig. 5c) and 30 min-etched Si (Fig. 5d), except for the aggregation of Si in the as-received sample.

EDX analyses on a 40×30 μm area of the electrode were conducted to detect the elemental change after cycling. Oxygen is a key element in both SiO_2 and the electrolyte decomposition products (such as, $-Si-OCH_2CH_2OCO_2Li$, $-Si-CH_2CH_2OCO_2Li$, $R(OCO_2Li)_2$, etc.). Thus, the change in atomic ratio between Si and O can be used to interpret the SEI formation in these electrodes. As summarized in Table III, O can be detected for fresh electrodes based on as-received Si due to the high SiO_2 content.

However, the O derived from SiO_2 in the etched sample is too low to be detected by EDX. After 1 cycle, the O content increases dramatically to 33.2 % for the electrode based on as-received Si and 29.2 % for the electrode based on 30 min-etched Si. The increase in O content must result from the products of electrolyte decomposition. The O contents in the two cycled electrodes are very similar after cycling, despite the surface oxide content between the as-received and 30 min-etch Si samples are different to start. This could imply a similar nature of SEI formed on the surface of the Si materials.
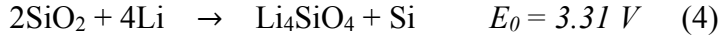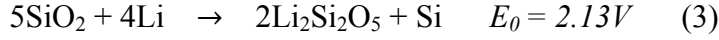
Role of electrolytes in the first cycle reaction. – The electrolyte must be considered in further understanding the first cycle reaction when a thick oxide layer is present on the surface of Si. The initial three lithiation dQ/dV curves for electrodes based on as-received Si are plotted in Fig. 6a. The electrode was lithiated and delithated using a small current density at 4.2 $\mu A\ cm^{-2}$ (0.01 C). One main peak at 1.64 V with other two peaks at 1.2 and 0.6 V are observed in the first lithiation process. The electrolyte used in this study is 1.2 M $LiPF_6$ in EC/DEC with 30 % FEC. To further assign the peaks, additional cells were made with EC/DEC electrolyte and pure FEC electrolyte, and cycled at 0.01C rate. The corresponding dQ/dV curves are shown in Fig.6b. Peaks at 1.6 V and 0.9 V are associated with the FEC electrolyte and EC/DEC electrolyte, respectively as seen in Fig. 6. There are also two small peaks at 1.2 and 0.6 V in Fig 6b, associated with FEC electrolyte but buried in the baseline due to the high intensity of the peak at 1.6 V (Fig. S-2). When a mixed electrolyte is used such as EC/DEC with 30% FEC, the major peak is related to an FEC induced reaction at 1.64 V that passivates the Si surface, preventing EC/DEC from reacting with the Si surface at a lower potential. This effect is very similar

to previous reports,[20] despite the thick SiO_2 layer present in this sample. If the reduction of SiO_2 were feasible in this potential range of 0.2-1 V, there would be an additional reduction peak at a similar position in all three electrolyte systems. The lack of this feature means that the SiO_2 reduction must happen in concurrence with lithiation of Si below 0.2 V during the first lithiation process.

Silicate formation at low potentials - The similarity of the electrode chemical change for the as-received and etched samples does not preclude SiO_2 reaction during the electrochemical process. XPS was used to investigate changes in the SiO_2 layer due to cycling of the electrode based on as-received Si. As shown in Fig. 7, the fresh electrode displays two peaks corresponding to stoichiometric SiO_2 (Si^{4+},105.2 eV) and elemental Si (Si^0,100.6 eV) in the Si $2p$ spectra (95 -110 eV binding energy region).[22, 23] A low current density of 4.5 µA cm^{-2} (0.01C) was applied to lithiate and delithiate the Si nanoparticles for two cycles.[24] After two lithiation/delithiation cycles, the electrode was stopped at the delithiation stage. The electrode was harvested, washed with DMC, and analyzed by XPS. The peaks assigned to SiO_2 and Si still can be observed for the electrode, although the peak has slightly shifted to a lower binding energy for Si^{4+}104.5 eV. Si^0 can be observed in the cycled electrode. The slight shifting of the Si^{4+} peak indicates that a possible reaction happened between SiO_2 and Li^+.

To facilitate this reaction, a similar electrode was cycled with a current of 4.2 µA cm^{-2} (0.01C) for 3 cycles, and then the cell was lithiated to 10 mV, and held for 194 h at this potential. The electrode was harvested at the lithiated stage. XPS analysis of this

11

electrode shows only one peak at 103 eV, which can be assigned to Li_4SiO_4[25] or

$Li_2Si_2O_5$[26] derived from the reduction of SiO_2, as shown in the following equations:

$$5SiO_2 + 4Li \rightarrow 2Li_2Si_2O_5 + Si \quad E_0 = 2.13V \quad (3)$$

$$2SiO_2 + 4Li \rightarrow Li_4SiO_4 + Si \quad E_0 = 3.31\ V \quad (4)$$

Thus, based on XPS data, the reduction of SiO_2 happens very slowly under normal

cycling conditions.[12] To enable the reaction, an extreme cycling condition has to be used,

such as applying a constant over-potential for a long period of time to drive the reaction

to completion. Both $Li_2Si_2O_5$ and Li_4SiO_4 are fairly stable between 0.01-1 V. Although

these silicates can be delithiated above 2V (Li/Li^+), the potential of a lithium-ion negative

electrode does not come close to 2V. The silicates are fairly stable after SiO_2 conversion;

however, this process consumes lithium ions. In a cell where lithium supply is limited,

this silicate formation will lead to a loss of capacity.

Characterization of bulk Si behavior. – Since the reduction of surface SiO_2 is a slow

process and subject to over-potential, a thick layer of SiO_2 is lithium-ion insulating

towards the Si core. Higher specific capacity can be achieved as the SiO_2 layer thickness

is systematically reduced. For as-received Si, the first delithiation capacity is 1320 mAh

g^{-1}. This value is increased to 2532 mAh g^{-1} for 10 min- etched Si. The electrode based

on 30 min- etched Si shows the highest delithiation capacity of 3309 mAh g^{-1}. (All three

capacity numbers are based on Si mass.) The increase of Si capacity is due to the

decrease in the insulating SiO_2 layer, which prevents lithium-ion alloying with Si core. In

order to confirm this, the Si particles were harvested from two electrodes based on as-

received and 30 min-etched Si nanoparticles after 1 round of lithiation and delithiation.

TEM images of the Si particles are shown in Fig. 8 along with pristine particle images before cycling for comparison. A 10 nm-thick SiO_2 layer was observed on the surface of as-received particles (Fig. 8a), and thickness of SiO_2 was reduced to 1-2 nm after 30 min of etching (Fig. 8d). An amorphous SiO_2 layer still can be observed on the as-received sample surface after cycling (Fig. 8b); moreover, nanocrystalline domains of Si are also observed (Fig. 8c). These nanocrystalline domains did not participate in the lithiation and delithation cycle, indicating that some parts of the Si core were insulated by a thick SiO_2 layer. However, for the etched Si nanoparticles with a thin SiO_2 layer, the Si core turned completely amorphous with one round of lithiation and delithiation (Fig. 8e and 8f). These TEM observations agree very well with the variation in reversible capacity observed for the as-received and etched samples.

In light of the distribution of the unreacted nanocrystalline Si domains in the as-received sample, and the over-potential needed to convert SiO_2 to silicate, a slow charge process should be able to access the untapped Si capacity. At a slow lithiation rate, the SiO_2 will convert to lithium-ion conducting silicate and there will be time for the slow solid-state lithium-ion diffusion to the Si domains. To confirm this hypothesis, the electrodes based on as-received Si were lithiated and delithiated at variable C-rates: 0.1C (94 μA cm^{-2}), 0.02C (20.8 μA cm^{-2}), and 0.01C (4.2 μA cm^{-2}). The delithiation capacity increased from 962 mAh g^{-1} at 0.1C to 1249 mAh g^{-1} at 0.02C and 1959 mAh g^{-1} at 0.01C lithiation rate, and the irreversible capacity also increased accordingly, presumably due to formation of lithium-ion conducting silicate (Fig. 9). (All three numbers are based on Si particle weight, including surface oxide.) The lithiation curve at a low current of 0.01C shows a

smaller over-potential compared with those at 0.1C and 0.02C. The turning point of potential plateau at 0.01C is about 0.05 V higher than that of the 0.1C.

Charge transfer impedances of the Si electrode. –The effect of the SiO_2 layer on the charge transfer impedance was investigated by performing electrochemical impedance spectroscopy (EIS) on a cell with an as-received Si electrode and another with a 30 min-etched Si electrode. The cells were cycled once, and then lithiated to 50% state of Si lithiation. . The results reflect the impedance of the entire test cell at different timescales. In the two types of cells studied, both Si and AB are active towards lithium-ion. In spite of the amount of AB being twice that of the Si nanoparticles and the surface area of AB dominating the electrode, AB has a small reversible specific capacity at 114 mAh/g. The EIS results of the two Si-based electrodes show distinct differences (Fig. 10).[27] There are at least 3 semicircles that can be resolved from the large semicirles in both cases, including the contribution of AB, Si, and the lithium counter-electrode. The combined interfacial resistance of the cell based on as-received Si is 5 times larger than that based on etched Si. The AB content and lithium counter electrode are identical in both cells; therefore, the contribution to the interfacial impedance is the same for both materials. When both of these factors are equally subtracted from the large semicircles, the 5 times difference of impedance between the as-received and etched sample becomes a conservative estimate.

Since the SEI formation is very similar for both electrodes as discussed previously, the resistance difference must be derived from the Si material itself. There are two variables

14

in the Si samples that affect the interfacial impedance: the SiO_2 layer thickness and the specific surface area. The specific surface area of the etched sample is about 3.5 times that of the as-received samples. Taking into account this correction factor for the EIS interfacial impedances between the two samples, the impedance from the as-received material is about 2X more than that of the etched samples. This remaining difference in interfacial resistance must originate from the SiO_2 layer thickness on the surface of the active materials. TEM has also shown that the SiO_2 layer is not uniform on the surface of as-received samples (Figure 1), and that the cycled samples have non-reactive Si nanodomains inside of the thick SiO_2 layers. Therefore, EIS measurements confirm that SiO_2 limits the active surface area for lithium-ion transport and increases the impedance of the electrode. This high interfacial impedance during the initial discharge process may cause the cell to reach the end of lithiation prematurely. This effect explains not only the low reversible capacity but also the high over-potential during the lithiation process for as-received Si-based electrodes (Fig. 8).

Conclusions

The SiO_2 layer on Si nanoparticles negatively affects the electrochemical performance of Si-based electrodes. After the first lithiation and delithiation process, nanocrystalline domains are still present in the Si nanoparticles that have a thick oxide layer. This surface SiO_2 layer is lithium-ion insulating, thereby slowing the lithium-ion transport at the SiO_2-Si interface and preventing the Si core from being lithiated. This insulating effect leads to a low reversible specific capacity and increases the interfacial charge transfer impedance. In addition, a larger initial capacity loss is found on the Si nanoparticles with

a thick oxide layer. Under normal cycling conditions, SiO_2 tends to react slowly with lithium-ions during lithiation; however when a constant low potential is applied to the electrode, this oxide layer can be quickly converted to the silicate form.   This transformation of the SiO_2 layer into a more stable and ion-conductive lithium silicate at 0.01-1 V (Li/Li^+) comes at the expense of the irreversible consumption of lithium-ions. This reaction leads to gradual loss of capacity in a lithium-ion cell. Therefore, HF etching of this oxide layer to make it thinner improves the electrochemical performance of Si-based electrodes. Understanding the effects of the Si native oxide layer on its electrochemical performance will benefit the design, modification, and manufacture of Si anodes for lithium-ion batteries.

Acknowledgments

Figure and Table Captions

Figure 1. TEM images of Si particles, (a) as-received and (b) after 30 min of HF etching. Scale bars: 100 nm.

Figure 2. FTIR spectra of Si particles before and after HF etching.

Figure 3. Specific capacity vs. cell voltage of the initial cycle of the electrodes based on as-received Si,10 min of HF etched Si and 30 min of HF etched Si.

Figure 4. dQ/dV differential curves of the first discharge profile (0.2 -2.2 V) based on as-received and 30 min-etched Si at 0.1C rate. (The feature below 0.2 V is a steep slope, and therefore is not included.)

Figure 5. SEM images of electrodes before cycling: (a) as-received Si and (b) 30 min-etched Si; after 1 cycle: (c) as-received Si and (d) 30 min-etched Si. Scale bars: 200 nm.

Figure 6. dQ/dV plots of electrodes based on as-received Si. (a) Initial three discharge curves with 1.2 M $LiPF_6$ in EC/DEC and 30 % FEC electrolyte. (b) First discharge curve with EC/DEC electrolyte (red) and with FEC electrolyte (black).

Figure 7. XPS spectra of the electrodes based on as-received Si. (a) Fresh electrodes, (b) after 2 cycles, (c) after 3.5 cycles and held at 10 mV for 194 hrs.

Figure 8. TEM images of Si particles. As-received: (a) without cycling and (b,c) after 1 cycle; after 30 min of HF etching: (d) without cycling and (e,f) after 1 cycle. Scale bars: 5 nm (a, c, d, f); and 50 nm (b and e).

Figure 9. The initial discharge/charge curves of electrodes based on as-received Si at different C rates.

Figure 10. Nyquist plots of the cells measured after 1 discharge/charge cycle with electrodes based on 30 min-etched Si and as-received Si.

Table I. Characterization of Si particles before and after HF etching.

Table II. First cycle capacity loss data.

Table III. The Si/O compositions (atomic %) of the electrodes as determined by EDX analysis on the surface.

References

1.   M. N. Obrovac and L. Christensen, Electrochem. Solid-State Lett. **7** (5), A93-A96 (2004).

2.   S. D. Beattie, D. Larcher, M. Morcrette, B. Simon and J. M. Tarascon, J. Electrochem. Soc. **155** (2), A158-A163 (2008).

3.   H. Li, X. J. Huang, L. Q. Chen, Z. G. Wu and Y. Liang, Electrochem. Solid-State Lett. **2** (11), 547-549 (1999).

4.   N. Ding, J. Xu, Y. X. Yao, G. Wegner, I. Lieberwirth and C. H. Chen, J. Power Sources **192** (2), 644-651 (2009).

5.   J. Graetz, C. C. Ahn, R. Yazami and B. Fultz, Electrochem. Solid-State Lett. **6** (9), A194-A197 (2003).

6.   J. Yang, M. Winter and J. O. Besenhard, Solid State Ionics **90** (1-4), 281-287 (1996).

7.   H. Kim, M. Seo, M. H. Park and J. Cho, Angew. Chem., Int. Ed. **49** (12), 2146-2149 (2010).

8.   T. L. Chan and J. R. Chelikowsky, Nano Lett. **10** (3), 821-825 (2010).

9.   H. Ma, F. Y. Cheng, J. Chen, J. Z. Zhao, C. S. Li, Z. L. Tao and J. Liang, Adv. Mater. **19** (22), 4067-+ (2007).

10.   A. Magasinski, P. Dixon, B. Hertzberg, A. Kvit, J. Ayala and G. Yushin, Nat. Mater. **9** (5), 461-461 (2010).

11.   H. Huang, E. M. Kelder, L. Chen and J. Schoonman, J. Power Sources **81**, 362-367 (1999).

12.   J. Saint, M. Morcrette, D. Larcher, L. Laffont, S. Beattie, J. P. Peres, D. Talaga, M. Couzi and J. M. Tarascon, Adv. Funct. Mater. **17** (11), 1765-1774 (2007).

13.   G. Bingkun, S. Jie, W. Zhaoxiang, Y. Hong, S. Lihong, L. Yinong and C. Liquan, Electrochem. Commun. **10**, 1876-1878 (2008).

14.   S. Qian, Z. Bing and F. Zheng-Wen, Appl. Surf. Sci. **254**, 3780-3785 (2008).

15.   S. Xun, X. Song, M. E. Grass, D. K. Roseguo, Z. Liu, V. S. Battaglia and G. Liu, Electrochem. Solid-State Lett. **14** (5), A61-A63 (2011).

16.   G. Liu, H. Zheng, S. Kim, Y. Deng, A. M. Minor, X. Song and V. S. Battaglia, J. Electrochem. Soc. **155** (12), A887-A892 (2008).

17. G. Liu, H. Zheng, A. S. Simens, A. M. Minor, X. Song and V. S. Battaglia, J. Electrochem. Soc. **154** (12), A1129-A1134 (2007).

18. R. D'Amato, M. Falconieri, F. Fabbri, M. Carpanese, F. Dumitrache and E. Borsella, 2008 Global Roadmap for Ceramics-ICC2 Proceedings, 597-600 (2008).

19. R. Hofman, J. G. F. Westheim, I. Pouwel, T. Fransen and P. J. Gellings, Surf. Interface Anal. **24** (1), 1-6 (1996).

20. N. S. Choi, K. H. Yew, K. Y. Lee, M. Sung, H. Kim and S. S. Kim, J. Power Sources **161** (2), 1254-1259 (2006).

21. P. F. McMillan and R. L. Remmele, Am. Mineral. **71** (5-6), 772-778 (1986).

22. M. Rossi, B. S. Mun, Y. Enta, C. S. Fadley, K. S. Lee, S. K. Kim, H. J. Shin, Z. Hussain and P. N. Ross, J. Appl. Phys. **103** (4), 044104 (2008).

23. Y. Enta, B. S. Mun, M. Rossi, P. N. Ross, Z. Hussain, C. S. Fadley, K. S. Lee and S. K. Kim, Appl. Phys. Lett. **92** (1), 012110 (2008).

24. N. Ariel, G. Ceder, D. R. Sadoway and E. A. Fitzgerald, J. Appl. Phys. **98** (2) (2005).

25. B. K. Guo, J. Shu, Z. X. Wang, H. Yang, L. H. Shi, Y. N. Liu and L. Q. Chen, Electrochem. Commun. **10** (12), 1876-1878 (2008).

26. Q. Sun, B. Zhang and Z. W. Fu, Appl. Surf. Sci. **254** (13), 3774-3779 (2008).

27. R. Ruffo, S. S. Hong, C. K. Chan, R. A. Huggins and Y. Cui, J. Phys. Chem. C **113** (26), 11390-11398 (2009).